Journal of Sound and Vibration (2000) **231**(1), 195–217
doi:10.1006/jsvi.1999.2660, available online at http://www.idealibrary.com on IDEAL®

LASER-BASED TRANSIENT SURFACE ACCELERATION OF THERMOELASTIC LAYERS

CETIN CETINKAYA, CUNLI WU AND CHEN LI

Department of Mechanical and Aeronautical Engineering, Clarkson University, Box 5725, Potsdam, NY 13699-5725, U.S.A.

(*Received* 18 *March* 1999, *and in final form* 27 *September* 1999)

The removal of particles from elastic substrates has been an important practical problem in the electronics industry especially as the sizes of electronic units shrink. In recent years, there has been an interest in removing *submicron* level particles from surfaces. The use of traditional surface cleaning methods, such as ultrasonically induced fluid flow, vibrational methods, centrifugal techniques, is limited to particles that require surface acceleration lower than $10^7\,\mathrm{m/s^2}$. For the effective removal of submicron particles, a higher level surface acceleration is needed since the adhesion forces (mainly van der Waals force for dry surfaces) are related to the particle size and increase approximately linearly as the characteristic radius of small particles that are to be removed decreases. In current work, based on the generalized dynamic theory of thermoelasticity reported, a transfer matrix formulation including the second sound effect is developed for a thermoelastic layer. The transfer matrix for axisymmetric wave propagation in a thermoelastic layer is obtained by adopting a double integral transform approach. The second sound effect is included to eliminate the thermal wave travelling with infinite velocity as predicted by the diffusion heat transfer model, and, consequently, the immediate arrival of waves. Using the current formulation and the periodic systems framework, a transfer function formulation for calculating the accelerations is developed for transient analysis. A double integral transform inversion method is used for transient response calculations. Acceleration levels, sufficient for submicron particle removal, are reported. Various processes such as thermoelastic stresses, surface evaporation, and optical breakdown may be responsible for surface acceleration components and particle removal. In current work, only the surface acceleration due to transient thermoelastic wave propagation is under investigation.

1. INTRODUCTION

Surface cleanness of substrates used in the electronic industry is one of the essential factors in circuit reliability. The removal of particles from elastic surfaces has increasingly become an important practical problem as the sizes of features in electronic components shrink at a high rate. In recent years, the focus of surface cleaning has been on the removal of *submicron* level particles.

The use of traditional surface motion-based surface cleaning methods, such as ultrasonically induced motion, vibrational methods, centrifugal techniques, is

0022-460X/00/110195 + 23 $35.00/0

mostly limited to particles that require surface acceleration lower than $10^7\,m/s^2$. For the effective removal of submicron particles, a higher level surface acceleration is needed since the adhesion forces (mainly van der Waals force for dry surfaces) increase approximately linearly as the minimum radius of particles that are to be removed decreases. A detailed account of surface acceleration mechanisms and reviews of other industrial techniques for various surface types are found in references [1, 2].

In current work, based on the generalized dynamic theory of thermoelasticity reported in reference [3], a transfer matrix formulation including the second sound effect is developed for a thermoelastic layer. For a historical perspective on developments in the second sound effect in solids, the reader is referred to a series of extensive review articles [4–7]. A more recent review on the topic can be found in reference [8]. In this study, the transfer matrix for axisymmetric wave propagation in a thermoelastic layer is obtained by utilizing a double integral transform method. The second sound effect, through a relaxation time term, is included to eliminate the thermal wave travelling with infinite velocity as predicted by the diffusion heat transfer model, and, consequently, the immediate arrival of waves. Similar transfer function formulations are utilized in reference [9] for calculating stress components due to laser beam excitation without considering a relaxation term, and in reference [10] for surface displacement calculations under laser heating. The transfer matrix formulation for axisymmetric elastic waves (without thermal effects) was given in reference [11]. The transfer matrix formulation has been used in various contexts (e.g., see references [12, 13] for its elegant use in layered structures) in elastic wave propagation since their introduction in the early 1950s [14, 15] in seismology. Using the current formulation and the periodic systems framework, a transfer function formulation for calculating the acceleration and temperature fields is developed for transient analysis (a recent detailed review on periodic systems research can be found in reference [16]). In the current study, a double integral transform inversion scheme based on the Fast Fourier Transform algorithm and Hankel transform is used for the transient analysis. It is found that acceleration levels are sufficient for submicron particles removal. As noted in reference [17], various processes such as thermoelastic stresses, surface evaporation, and optical breakdown may be responsible for surface acceleration. Here only the surface acceleration, due to transient thermoelastic wave propagation generated by a heating source, is under investigation. No detailed temperature result is presented in the current work; however, preliminary numerical work indicated that the temperature increase on the surface is low compared to the melting point of the layer material. In a finite element study [18], a similar level of temperature increase is reported.

Recent advances in photonics and laser instrumentation (such as pulsed laser, laser interferometry, and fiber optics) and price structure in industry have been creating a favorable environment for thermal-based elastic wave generation techniques and their applications in various fields, such as non-destructive testing, smart structures, and surface cleaning.

The inverse problem, namely, the study of the characteristics of the adhesion between the surface and particle, can also be of practical interest. The current

formulation along with experimental interferometric data can be used in a detailed characterization of bonding for various surface and particle materials.

2. FORMULATION

"In an idealized solid, thermal energy is transported by two different mechanisms: the quantitized electronic excitations, which are called free electrons, and the quanta of lattice vibrations, which are called phonons. These quanta undergo collisions of a dissipative nature, giving rise to thermal resistance in the medium. A relaxation time τ_0 is associated with the average communication time between these collisions for the commencement of resistive flow" [6]). In the following formulation, this relaxation effect is taken into account in order to eliminate the infinite thermal wave propagation speed paradox.

The linearized governing equations for the displacement, **u**, and absolute temperature, T, fields for a homogeneous medium consist of two coupled partial differential equations, the (Navier's) equation of motion and the energy equation:

$$(\lambda + 2\mu)\nabla(\nabla \cdot \mathbf{u}) - \mu\nabla \times (\nabla \times \mathbf{u}) - \beta\nabla T + \rho_0(\mathbf{f} - \ddot{\mathbf{u}}) = 0, \tag{1}$$

$$-\kappa\nabla^2 T - \rho_0 h + T_0\beta\nabla \cdot (\dot{\mathbf{u}} + \tau_0\ddot{\mathbf{u}}) + \rho_0\gamma(\dot{T} + \tau_0\ddot{T}) = 0, \tag{2}$$

where λ and μ are Lamé constants of the layer material, ρ_0 is the layer material density, κ is the thermal conductivity, γ is the specific heat capacity, h is the internal heat source intensity, T_0 is the temperature at the normal state, τ_0 is the relaxation time, and overdot represents time-derivative, and β is the thermo-elastic coupling:

$$\beta = 3(\lambda + \tfrac{2}{3}\mu)\alpha,$$

where α is the thermal expansion coefficient. The relaxation time τ_0 "represents the time-lag needed to establish steady state heat conduction in an element of volume when a temperature gradient is suddenly imposed on that element" [3].

These coupled equations are complemented by the following constitutive relation and Fourier's law for isotropic materials:

$$\sigma_{ij} = -\beta T\delta_{ij} + \lambda u_{n,n}\delta_{ij} + \mu(u_{i,j} + u_{j,i}), \qquad q_i + \tau_0\dot{q}_i = -\kappa T_{,i}, \tag{3, 4}$$

where σ_{ij} is the stress tensor, q_i is the heat flux in the direction i, δ_{ij} is the Kronecker delta, and the index following the comma in the subscript indicates differentiation with respect to corresponding co-ordinate. These expressions constitute the generalized dynamic theory of linear thermoelasticity which was first proposed in reference [3].

Unlike the classical heat equation which is a parabolic partial differential equation in the generalized theory, the energy equation (2) contains a term with $\ddot{T}$ which makes it a hyperbolic equation as the displacement equation (1). This solves the problem of infinite speed thermal wave propagation predicted by the

heat diffusion equation. The propagation of thermal waves, the second sound effect, was first postulated by Maxwell [19] in 1867 on the physical argument that heat pulses cannot propagate with infinite velocity in matter. For the first time, Peshkov [20] experimentally demonstrated that thermal waves propagate at finite velocity in liquid Helium in 1944. However, the experimental verification in solids is still largely an open problem (e.g., cf. references [6, 7]).

An approximation for the relaxation time for metallic materials is given in reference [21] as

$$\tau_0 \simeq \frac{3\kappa}{(\lambda + 2\mu)\gamma}. \tag{5}$$

Using this approximation, a speed for thermal wave propagation is obtained:

$$c_a \simeq \sqrt{\frac{\kappa}{\rho\gamma\tau_0}} = \frac{c_L}{\sqrt{3}}. \tag{6}$$

The first step in generating a transfer matrix formulation for a thermoelastic layer is to adopt the Helmholtz decomposition for the displacement field into the scalar, ϕ, and vector, $\boldsymbol{\varphi}$, potentials functions:

$$\mathbf{u} = \nabla\phi + \nabla \times \boldsymbol{\varphi}, \tag{7}$$

and the body force field is also decomposed into the scalar, g, and vector, $\mathbf{h}$, components

$$\mathbf{f} = -\nabla g - \nabla \times \mathbf{h} \tag{8}$$

with the gauge conditions that are required to eliminate the problem of over-determinedness of the field variables:

$$\nabla \cdot \boldsymbol{\varphi} = \nabla \cdot \mathbf{h} = 0. \tag{9}$$

Representing equations (1)–(4) in terms of these potential functions results in three wave equations (one of which is decoupled) in the (vector and scalar) displacement potentials and temperature:

$$c_L^2 \nabla^2 \phi - \frac{\beta}{\rho_0} T - g - \ddot{\phi} = 0, \tag{10}$$

$$c_T^2 \nabla \times \nabla \times \boldsymbol{\varphi} + \mathbf{h} + \ddot{\boldsymbol{\varphi}} = 0, \tag{11}$$

$$-\kappa\nabla^2 T - \rho_0 h + T_0 \beta \nabla^2(\dot{\phi} + \tau_0 \ddot{\phi}) + \rho_0 \gamma(\dot{T} + \tau_0 \ddot{T}) = 0, \tag{12}$$

where $c_L^2 = (\lambda + 2\mu)/\rho_0$ and $c_T^2 = \mu/\rho_0$ (c_L and c_T, are, respectively, the propagation speeds of irrotational isothermal and equivoluminal isothermal waves in anisotropic medium). In the absence of body forces, $g = 0$ and $\mathbf{h} = \{0, 0, 0\}^{\mathrm{T}}$, the wave

field in cylindrical co-ordinates can be studied by considering only two potential function components since some shear stress components diminish due to the axisymmetry of the wave field: the scaled potential, ϕ, and the radial potential vector component, φ_θ. After adopting the non-dimensional variables

$$\Psi = \frac{\varphi_\theta}{H}, \qquad \Phi = \frac{\phi}{H}, \qquad \tau = \frac{c_T}{H}t, \qquad \rho = \frac{r}{H}, \qquad \xi = \frac{z}{H}, \tag{13}$$

where H is a characteristic distance (later the layer thickness will be used), t is the time, z is the axial co-ordinate, and r is the radial co-ordinate. The Fourier transform in τ, the scaled time, and Hankel transform of order zero in ρ, the scaled radial co-ordinate, for the initial conditions are

$$\Psi = \Phi = \frac{\partial \Phi}{\partial t} = \frac{\partial \Psi}{\partial t} = \frac{\partial \Phi}{\partial r} = \frac{\partial \Psi}{\partial r} = \frac{\partial \Phi}{\partial z} = \frac{\partial \Psi}{\partial z} = 0, \text{ everywhere at } t = 0. \tag{14}$$

Equation (10) can be written as

$$b_1 \bar{\Phi}^0 + \frac{\mathrm{d}^2 \bar{\Phi}^0}{\mathrm{d}\xi^2} + b_2 \bar{T}^0 = 0, \tag{15}$$

where $b_1 = -(k^2 + (c_L^2/c_T^2)p^2)$, $b_2 = -(H\beta/c_L^2\rho_0)$, p and k are the Laplace variable and the scaled radial wave number, the overbar stands for the Laplace transformed state variable, and the superscript 0 is for the zeroth order Hankel transformed quantity. With the Fourier transform in τ and Hankel transform of order one in ρ, equation (11) becomes

$$-(k^2 + p^2)\bar{\Psi}^1 + \frac{\mathrm{d}^2 \bar{\Psi}^1}{\mathrm{d}\xi^2} = 0, \tag{16}$$

where superscript 1 is for the first order Hankel transformed quantity. Finally the Fourier transform in τ and Hankel transform of order zero in ρ, equation (12), can be obtained in the form

$$a_1 \bar{T}^0 + a_2 \bar{\Phi}^0 + a_3 \frac{\mathrm{d}^2 \bar{\Phi}^0}{\mathrm{d}\xi^2} + a_4 \frac{\mathrm{d}^2 \bar{T}^0}{\mathrm{d}\xi^2} = 0, \tag{17}$$

where

$$a_1 = \frac{\kappa}{H^2}k^2 + \left(1 + \frac{c_T}{H}p\tau_0\right)\rho_0\gamma\frac{c_T}{H}p, \quad a_3 = \left(1 + \frac{c_T}{H}p\tau_0\right)T_0\beta\frac{c_T}{H^2}p, \tag{18}$$

$$a_2 = -\left(1 + \frac{c_T}{H}p\tau_0\right)T_0\beta\frac{c_T}{H^2}pk^2, \quad a_4 = -\frac{\kappa}{H^2}. \tag{19}$$

In these equations, the potential function $\bar{\Psi}^1$ is decoupled from $\bar{\Phi}^0$ and $\bar{T}^0$. Since only the *P*-wave causes the volume change, $\bar{\Phi}^0$ and $\bar{T}^0$ are functionally related. $\bar{\Psi}^1$ corresponds to the equivoluminal motion, and therefore it has no effect on the thermal terms. The solution to $\bar{\Psi}^1$ from equation (16) is

$$\bar{\Psi}^1 = B_1(p,k)\mathrm{e}^{-h\xi} + B_2(p,k)\mathrm{e}^{h\xi}, \tag{20}$$

where $h = \sqrt{k^2 + p^2}$, and $B_1(p,k)$ and $B_2(p,k)$ are integration constants. Similarly, solving equations (15) and (17) simultaneously yields the solutions to the temperature and scalar potential functions:

$$\begin{aligned}\bar{T}^0 = {} & A_1(p,k)C_1(p,k)\mathrm{e}^{-c_1\xi} - A_2(p,k)C_1(p,k)\mathrm{e}^{c_1\xi} \\ & + A_3(p,k)C_2(p,k)\mathrm{e}^{-d_1\xi} - A_4(p,k)C_2(p,k)\mathrm{e}^{d_1\xi},\end{aligned} \tag{21}$$

$$\begin{aligned}\bar{\Phi}^0 = {} & A_1(p,k)E_1(p,k)\mathrm{e}^{-c_1\xi} - A_2(p,k)E_1(p,k)\mathrm{e}^{c_1\xi} \\ & + A_3(p,k)E_2(p,k)\mathrm{e}^{-d_1\xi} - A_4(p,k)E_2(p,k)\mathrm{e}^{d_1\xi},\end{aligned} \tag{22}$$

where $A_1(p,k)$, $A_2(p,k)$, $A_3(p,k)$, and $A_4(p,k)$ are integration constants, and the other terms are obtained as

$$c_1 = \sqrt{\frac{m_1 - \sqrt{m_2}}{2a_4}}, \quad m_1 \triangleq -a_1 - a_4 b_1 + a_3 b_2,$$

$$d_1 = \sqrt{\frac{m_1 + \sqrt{m_2}}{2a_4}}, \quad m_2 \triangleq -4a_4(a_1 b_1 - a_2 b_2) + m,$$

$$C_1(p,k) = -\frac{1}{b_2}\left(c_1 + \frac{b_1}{c_1}\right), \quad E_1(p,k) = -\frac{1}{c_1},$$

$$C_2(p,k) = -\frac{1}{b_2}\left(d_1 + \frac{b_1}{d_1}\right), \quad E_2(p,k) = -\frac{1}{d_1}.$$

The modified heat conduction law of Fourier for the second sound effect in the ξ direction after the Fourier transform becomes

$$\bar{q}_\xi^0 = \frac{-\kappa}{(1 + \tau_0 p)H}\frac{\mathrm{d}\bar{T}^0}{\mathrm{d}\xi}. \tag{23}$$

From equations (3) and (7), the transformed displacements and stress components in terms of the potential functions and the temperature are represented as

$$\bar{u}_\rho^1 = -\left(k\bar{\Phi}^0 + \frac{\mathrm{d}\bar{\Psi}^1}{\mathrm{d}\xi}\right), \qquad \bar{u}_\xi^0 = \frac{\mathrm{d}\bar{\Phi}^0}{\mathrm{d}\xi} + k\bar{\Psi}^1, \tag{24, 25}$$

$$\bar{\sigma}^0_{\xi\xi} = -\lambda k^2 \bar{\Phi}^0 + (\lambda + 2\mu)\frac{\mathrm{d}^2\bar{\Phi}^0}{\mathrm{d}\xi^2} + 2\mu k\frac{\mathrm{d}\bar{\Psi}^1}{\mathrm{d}\xi} - \beta\bar{T}^0, \tag{26}$$

$$\bar{\sigma}^1_{\xi\rho} = -\mu\left(2k\frac{\mathrm{d}\bar{\Phi}^0}{\mathrm{d}\xi} + \frac{\mathrm{d}^2\bar{\Psi}^1}{\mathrm{d}\xi^2} + k^2\bar{\Psi}^1\right). \tag{27}$$

Substituting the scalar potential and temperature fields into these heat, displacement and stress components in potential functions, a six-by-six transfer matrix formulation for the integration constants, B_1, B_2, E_1A_1, E_1A_2, E_2A_3 and E_2A_4 is obtained:

$$[T(\xi)]\{B_1 \;\; B_2 \;\; E_1A_1 \;\; E_1A_2 \;\; E_2A_3 \;\; -E_2A_4\}^{\mathrm{T}} = \{\bar{u}^1_\rho \;\; \bar{u}^0_\xi \;\; \bar{\sigma}^0_{\xi\xi} \;\; \bar{\sigma}^1_{\xi\rho} \;\; \bar{T}^0 \;\; \bar{q}^0_\xi\}^{\mathrm{T}}, \tag{28}$$

where

$$[T(\xi)] = \begin{bmatrix} [T_{11}] & [T_{12}] & [T_{13}] \\ [T_{21}] & [T_{22}] & [T_{23}] \\ [T_{31}] & [T_{32}] & [T_{33}] \end{bmatrix}. \tag{29}$$

Submatrices $[T_{ij}]$ are given as

$$[T_{11}] = \begin{bmatrix} h\mathrm{e}^{-h\xi} & -h\mathrm{e}^{h\xi} \\ k\mathrm{e}^{-h\xi} & k\mathrm{e}^{h\xi} \end{bmatrix}, \quad [T_{12}] = \begin{bmatrix} -k\mathrm{e}^{-c_1\xi} & k\mathrm{e}^{c_1\xi} \\ -c_1\mathrm{e}^{-c_1\xi} & -c_1\mathrm{e}^{c_1\xi} \end{bmatrix},$$

$$[T_{13}] = \begin{bmatrix} -k\mathrm{e}^{-d_1\xi} & -k\mathrm{e}^{d_1\xi} \\ -d_1\mathrm{e}^{-d_1\xi} & d_1\mathrm{e}^{d_1\xi} \end{bmatrix},$$

$$[T_{21}] = \begin{bmatrix} -2\mu kh\mathrm{e}^{-h\xi} & 2\mu kh\mathrm{e}^{h\xi} \\ -\mu(h^2+k^2)\mathrm{e}^{-h\xi} & -\mu(h^2+k^2)\mathrm{e}^{h\xi} \end{bmatrix},$$

$$[T_{22}] = \begin{bmatrix} ((\lambda+2\mu)c_1^2 - \lambda k^2)\mathrm{e}^{-c_1\xi} & (\lambda k^2 - (\lambda+2\mu)c_1^2)\mathrm{e}^{c_1\xi} \\ 2\mu kc_1\mathrm{e}^{-c_1\xi} & 2\mu kc_1\mathrm{e}^{c_1\xi} \end{bmatrix},$$

$$[T_{23}] = \begin{bmatrix} ((\lambda+2\mu)d_1^2 - \lambda k^2)\mathrm{e}^{-d_1\xi} & -(\lambda k^2 + (\lambda+2\mu)d_1^2)\mathrm{e}^{d_1\xi} \\ 2\mu kd_1\mathrm{e}^{-d_1\xi} & -2\mu kd_1\mathrm{e}^{d_1\xi} \end{bmatrix},$$

$$[T_{31}] = \begin{bmatrix} 0 & 0 \\ 0 & 0 \end{bmatrix},$$

$$[T_{32}] = \begin{bmatrix} C_{e_1}\mathrm{e}^{-c_1\xi} & -C_{e_1}\mathrm{e}^{c_1\xi} \\ \dfrac{\kappa}{H}C_{e_1}c_1\mathrm{e}^{-c_1\xi} & \dfrac{\kappa}{H}C_{e_1}c_1\mathrm{e}^{c_1\xi} \end{bmatrix}, \quad [T_{33}] = \begin{bmatrix} C_{e_2}\mathrm{e}^{-d_1\xi} & C_{e_2}\mathrm{e}^{d_1\xi} \\ \dfrac{\kappa}{H}C_{e_2}d_1\mathrm{e}^{-d_1\xi} & -\dfrac{\kappa}{H}C_{e_2}d_1\mathrm{e}^{d_1\xi} \end{bmatrix},$$

where $C_{e_1} = C_1/E_1$, $C_{e_2} = C_2/E_2$, the superscript T stands for the transpose operation.

By inspection, the matrix $[T(\xi)]$ is decomposed into a multiplication of two matrices:

$$[T(\xi)] = [T(0)]\, diag(\mathrm{e}^{-h\xi}, \mathrm{e}^{h\xi}, \mathrm{e}^{-c_1\xi}, \mathrm{e}^{c_1\xi}, \mathrm{e}^{-d_1\xi}, \mathrm{e}^{d_1\xi}). \tag{30}$$

where *diag*( ) stands for the diagonal matrix whose diagonal entries are its arguments, and

$$[T(0)] =$$

$$\begin{bmatrix}
h & -h & -k & k & -k & -k \\
k & k & -c_1 & -c_1 & -d_1 & d_1 \\
-2\mu kh & 2\mu kh & -\lambda k^2 + (\lambda + 2\mu)c_1^2 & \lambda k^2 - (\lambda + 2\mu)c_1^2 & -\lambda k^2 + (\lambda + 2\mu)d_1^2 & -\lambda k^2 - (\lambda + 2\mu)d_1^2 \\
-\mu(h^2 + k^2) & -\mu(h^2 + k^2) & 2\mu kc_1 & 2\mu kc_1 & 2\mu kd_1 & -2\mu kd_1 \\
0 & 0 & C_{e_1} & -C_{e_1} & C_{e_2} & C_{e_2} \\
0 & 0 & \frac{\kappa}{H} C_{e_1} c_1 & \frac{\kappa}{H} C_{e_1} e_1 & \frac{\kappa}{H} C_{e_2} d_1 & -\frac{\kappa}{H} C_{e_2} d_1
\end{bmatrix}$$

From equation (28), the boundary conditions on the top and the bottom surfaces of a thermoelastic layer become

$$[T(0)]\{B_1 \;\; B_2 \;\; E_1A_1 \;\; E_1A_2 \;\; E_2A_3 \;\; -E_2A_4\}^{\mathrm{T}} = \{S\}_L, \text{ at } \xi = 0, \tag{31}$$

$$[T(1)]\{B_1 \;\; B_2 \;\; E_1A_1 \;\; E_1A_2 \;\; E_2A_3 \;\; -E_2A_4\}^{\mathrm{T}} = \{S\}_R, \text{ at } \xi = 1, \tag{32}$$

where the thermoelastic state vectors are

$$\{S\}_L = \{\bar{u}_\rho^1 \;\; \bar{u}_\xi^0 \;\; \bar{\sigma}_{\xi\xi}^0 \;\; \bar{\sigma}_{\xi\rho}^1 \;\; \bar{T}^0 \;\; \bar{q}_\xi^0\}_L^{\mathrm{T}}, \quad \{S\}_R = \{\bar{u}_\rho^1 \;\; \bar{u}_\xi^0 \;\; \bar{\sigma}_{\xi\xi}^0 \;\; \bar{\sigma}_{\xi\rho}^1 \;\; \bar{T}^0 \;\; \bar{q}_\xi^0\}_R^{\mathrm{T}}.$$

By eliminating the integration constants in equations (31) and (32), the following matrix equation relating the displacement, stress and thermal state at the two surfaces of a layer with a thickness H is obtained:

$$\{S\}_R = [T_{layer}]\{S\}_L, \tag{33}$$

where $[T_{layer}] = [T(1)]\,[T(0)]^{-1}$. The coefficient matrix on the left-hand side of equation (33), namely $[T(1)]\,[T(0)]^{-1}$, can be written as $[T(0)][\Lambda][T(0)]^{-1}$ which implies a similarity transformation between the transfer matrix for a layer and the matrix $[\Lambda]$. Since the matrix $[\Lambda]$ is diagonal, the entries of this matrix are the eigenvalues of the transfer matrix and the columns of $[T(0)]$, therefore,

TABLE 1

Material thermoelastic properties and thicknesses of the layers (Systems I and II). The two layers differ only in the layer thicknesses

Systems I and II
$E = 310{\cdot}3\,\text{GPa}$
$\rho_0 = 3248{\cdot}8\,\text{kg/m}^3$
$\lambda = 124{\cdot}1\,\text{GPa}$
$\mu = 124{\cdot}1\,\text{GPa}$
$H_1 = 3{\cdot}125 \times 10^{-3}\,\text{m}$ for System I
$H_{11} = 6{\cdot}25 \times 10^{-3}\,\text{m}$ for System II
$v = 0{\cdot}25$
$c_L = 10705{\cdot}2\,\text{m/s}$
$c_T = 6180{\cdot}6\,\text{m/s}$
$\kappa = 403\,\text{W/m K}$
$\gamma = 390\,\text{J/kg K}$
$\beta = 1{\cdot}0394 \times 10^7$
$\tau_0 = 8{\cdot}322 \times 10^{-12}\,\text{s}$

correspond to the eigenvectors of the transfer matrix $[T_{layer}]$. In monitoring and controlling the inherent numerical instabilities (loss of precision) in the hyperbolic transfer matrices, an accurate calculation of the condition number is important and, for the transfer matrix $[T_{layer}]$, it is the maximum of $c^{2|c_1|}$ or $e^{2|d_1|}$ due to equation (30).

3. THERMOELASTIC TRANSIENT RESPONSE

Once the transfer matrix is developed, it is straightforward to calculate the transfer function between the applied thermal field on a circular area on a surface of the layer and any other state variable (see equations (31) and (32)) at any point in the layer (inside or on a surface of the layer). The condition number for the transfer matrix is the maximum of $e^{2|c_1|}$ or $e^{2|d_1|}$. With this knowledge at hand, the inherent numerical instability problem can be monitored and controlled without introducing considerable error. In this study, the axial and radial transient acceleration components in two thermoelastic structures (Systems I and II) with different thicknesses are computed at eight station points. The material thermoelastic properties and thicknesses of the layers for Systems I and II are listed in Table 1. The layer material properties are for a metallic material. Note that the two systems differ only in the layer thicknesses. The locations of these eight points are depicted in Figure 1 for $r_0 = 5\,\text{mm}$.

In the transient response simulations, the maximum radial frequency (Nyquest frequency) in the transfer function computations is 0·79 GHz for both Systems I and II. This frequency range covers more than 50 natural frequencies. The maximum value of the radial wavenumbers, k_{max}, for System I is $32\,000\,\text{m}^{-1}$

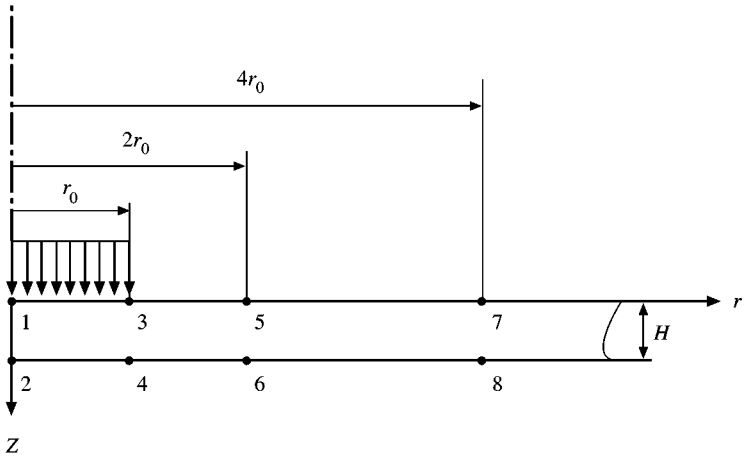

Figure 1. Cross-section of a layer showing the eight station points at which axial and radial components of the acceleration vector are computed ($r_0 = 5$ mm).

(corresponding minimum wavelength $\lambda_{min} = 0{\cdot}31$ mm) for the upper surface (where the laser heating is applied) and is $20\,800\,\mathrm{m}^{-1}$ (corresponding minimum wavelength $\lambda_{min} = 0{\cdot}48$ mm) for the lower surface. The maximum value of the radial wavenumber, k_{max}, for System II is $25\,600\,\mathrm{m}^{-1}$ (corresponding minimum wavelength $\lambda_{min} = 0{\cdot}39$ mm) for both the upper and lower surfaces of the layer. These values are dictated mainly by the power spectrum (Figures 2(a–b)) and the Hankel transforms of the spatial component of the input heating function (Figures 3(a–c)).

Systems I and II are excited by a temporal-spatial thermal field on the top surfaces:

$$q_z = f_1(t) f_2(r).$$

The heat flow mimics a laser-based heating. While most laser beams provide Gaussian-type distribution, for simplicity, in the simulations the temporal dependency of the applied heat field is trapezoidal (Figure 2(a)), and the spacial dependency is a step function with a 5-mm radius support (Figure 3(a)). In case of a Gaussian-type distribution, the power spectrum of the function $f_1(t)$ will be different. No other laser effects (such as surface evaporation and optical breakdown) are considered in these simulations. The power spectrum of the time-dependent part of the excitation is given in Figure 2(b). The zeroth and first order Hankel transforms of the spatial-dependent part are given in Figures 3(b) and (c). These figures along with the transfer functions are used to determine the Nyquest frequency and the maximum wave number for the excitation. Free-free boundary conditions are imposed in calculating transfer functions. The numerical simulations are based on the Fast Fourier Transform algorithm and an inverse Hankel transform scheme. Various sampling rates ranging from 10^5 to 10^7 are used for the required resolution in order to obtain physically meaningful results. In some cases,

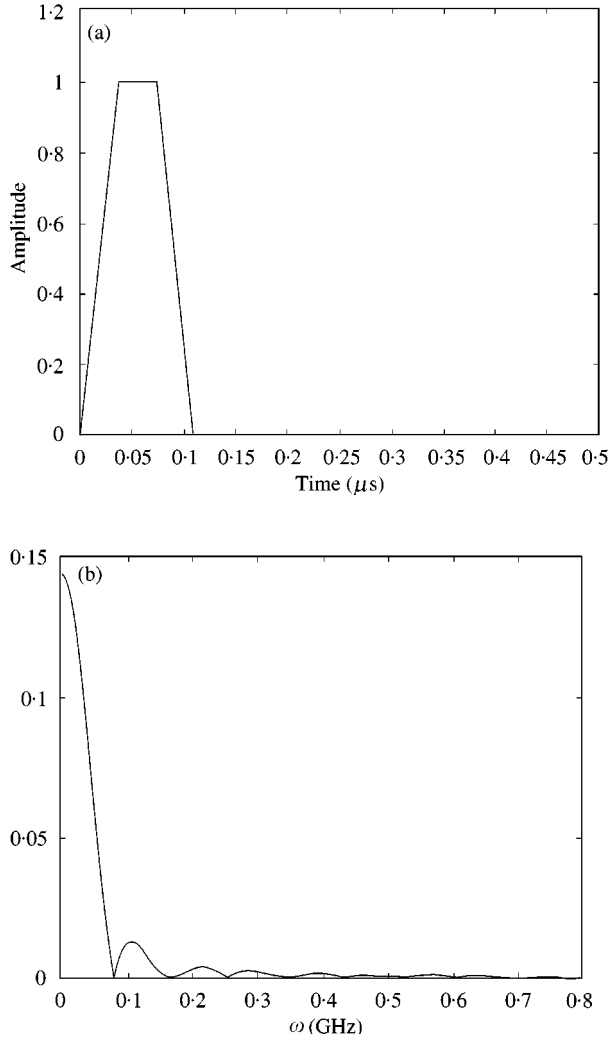

Figure 2. (a) Applied thermal field (heat flux) in time, $f_1(t)$, and (b) its power spectrum.

a material damping is used to minimize the effect of excessive sampling requirements around the resonance frequencies. Commonly used values for material damping were in the range of 1–5%. As previously noted, in the case of thermoelastic wave propagation, the need for material damping is less severe than the purely elastic case since the coupling between the displacement and temperature fields provides mode conversion attenuation.

In Figure 4, the axial acceleration (in the z direction) at Station 1 for the two systems is compared. Due to axisymmetry, there is no radial acceleration at Station 1. Regardless of the layer thickness, the maximum and minimum acceleration levels are about the same for both systems, since the thermoelastic wave field is nearly one-dimensional in the early times (compared to the travel times needed to observe

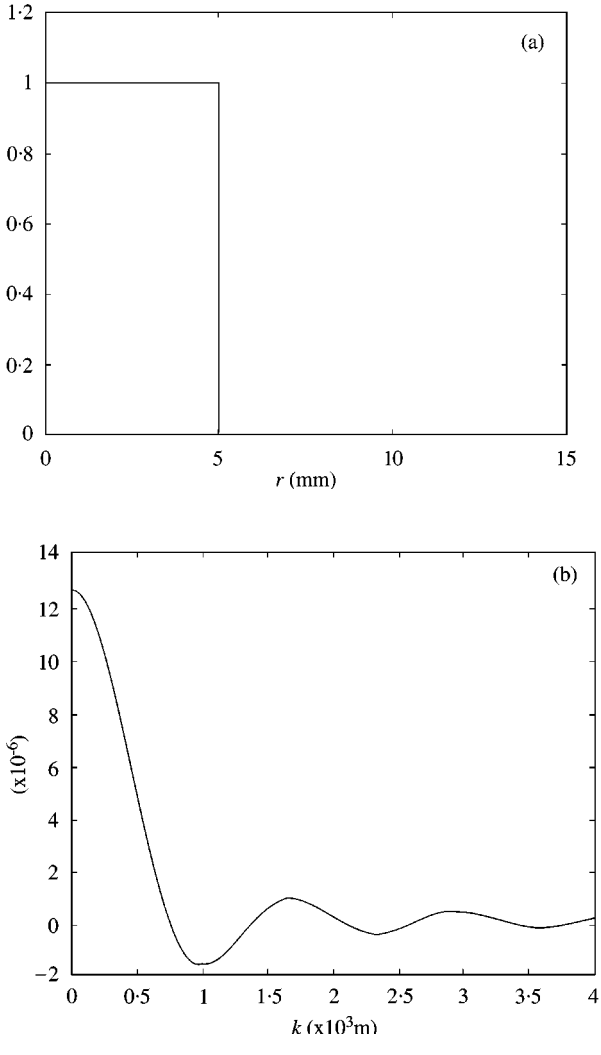

Figure 3. (a) Applied field in the radial co-ordinate r, $f_2(r)$, (b) its zeroth and (c) first order Hankel transforms.

the dimensionality of the input functions). The high-frequency component superimposed on the response of System II in Figure 4 is more likely a numerical error which comes from a lightly damped natural frequency.

At Station 2, the difference in the maximum and minimum acceleration levels is becoming visible. The arrival of the wave front in System I is stronger than that in System II. The calculated arrival time for System I at Station 2 is approximately 0·29 μs. The arrival times in Figure 5 are in agreement with the calculated values for both systems. In Figures 6(a) and (b) both components of the acceleration are presented. While the extremum values of the axial acceleration in both systems are very close to each other, the radial acceleration in System I is nearly twice as much

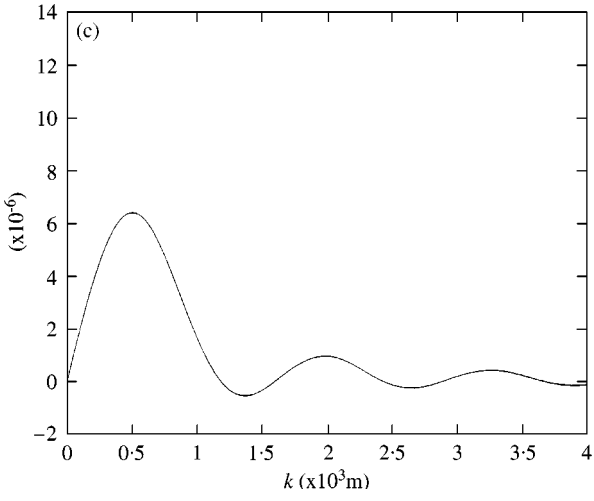

Figure 3. Continued

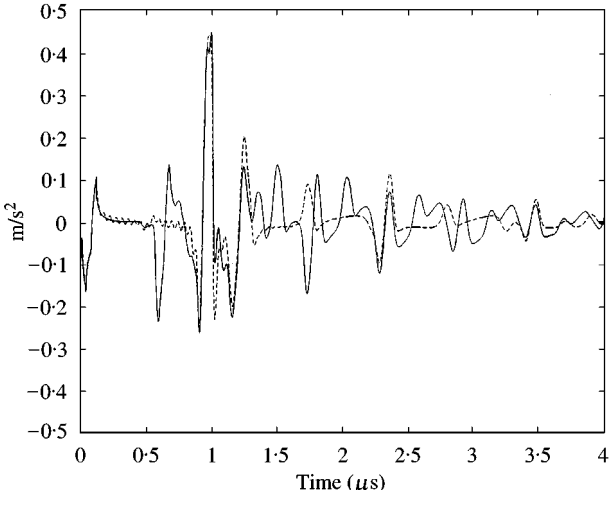

Figure 4. Acceleration in the z direction versus time for Systems I (—) and II (· · · · ·) at station point 1.

as that in System II in the first 2·0 μs time period (Figure 7). After this time period, the acceleration levels in both systems differ very little.

At Station 4, the axial acceleration levels in System I are 10–15% more that in System II, and the radial acceleration in System I is 60–70% more that in System II. At station 5, the acceleration levels for both systems differ very little. The arrival time at Station 5 is approximately 0·47 μs as one can observe in Figures 8(a) and (b). The arrival of the wave front is more visible in the radial acceleration results. The difference in the extremum values of the accelerations is in the range of 5–10%.

From Stations 3 to 5, a large reduction in acceleration (up to 75%) is observed, even though the distance between the two stations is 5 mm. In Figures 8(a) and (b), it is clear that the large wave front acceleration is due to a Rayleigh and/or shear wave component.

The difference between acceleration levels nearly diminish at Station 6 (Figures 9(a) and (b)). It appears that the only effect layer thickness causes is on the arrival times far away from the heated region. This observation is supported by the response at Stations 7 and 8 further depicted in Figures 10(a) and (b) and 11(a, b).

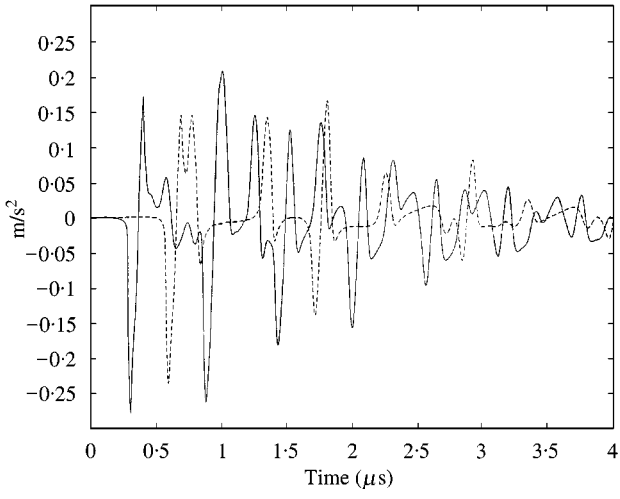

Figure 5. Acceleration in the z direction versus time for Systems I (—) and II (·····) at station point 2.

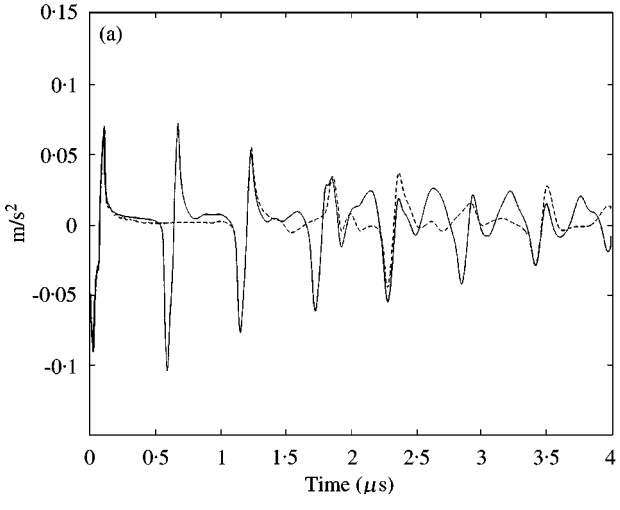

Figure 6. Acceleration versus time (a) in the z direction (b) in the radial direction r for Systems I (—) and II (····) at station 3.

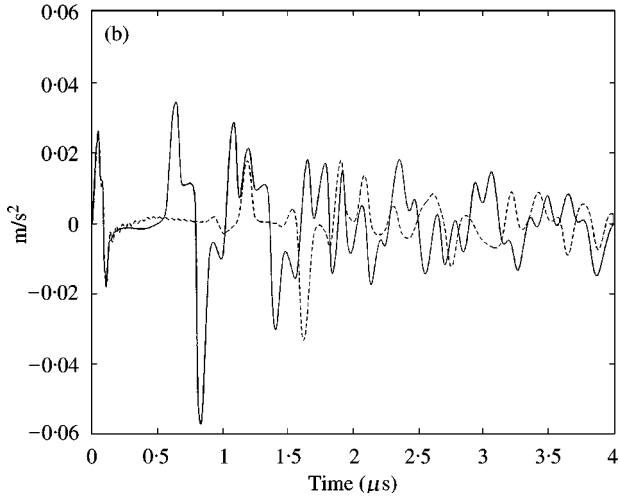

Figure 6. Continued

In Figures 12(a, b) and 13(a, b), the change of the maximum and minimum acceleration levels as a function of the station location is summarized.

4. LASER PULSE ENERGY

In pulsed lasers, the pulse energy is listed as a performance specification, and it typically varies from a few mJ (milli Joule) to few Joule levels. Results reported in Figures 5–13 are generated for a pulse with unit amplitude, and so they can be used for a laser with various pulse energies. For this normalization the following scaling factor is derived by considering the energy under the area of the trapezoidal pulse in time:

$$q = \frac{2Q_0}{\pi r_0^2(c + b - a)},$$

where Q_0 is the pulse energy of the laser, r_0 is the radius of the laser beam, a, $(b - a)$ and $(c - b)$ are, respectively, the time interval for inclining, plateau, and declining portions of the trapezoid. The pulse duration is specified by c. For example, the normalization factor q for a laser with pulse energy $Q_0 = 50\,\text{mJ}$ is approximately $8{\cdot}8 \times 10^9$. Thus, from Figures 12 and 13, the maximum acceleration levels are determined to be in the order of 10^9 for such a laser.

5. CONCLUSIONS AND REMARKS

A six-by-six axisymmetric transfer matrix formulation for an thermoelastic layer is generated. The formulation includes the second sound effect (through the relaxation term in both the equations of motion and energy) to eliminate the

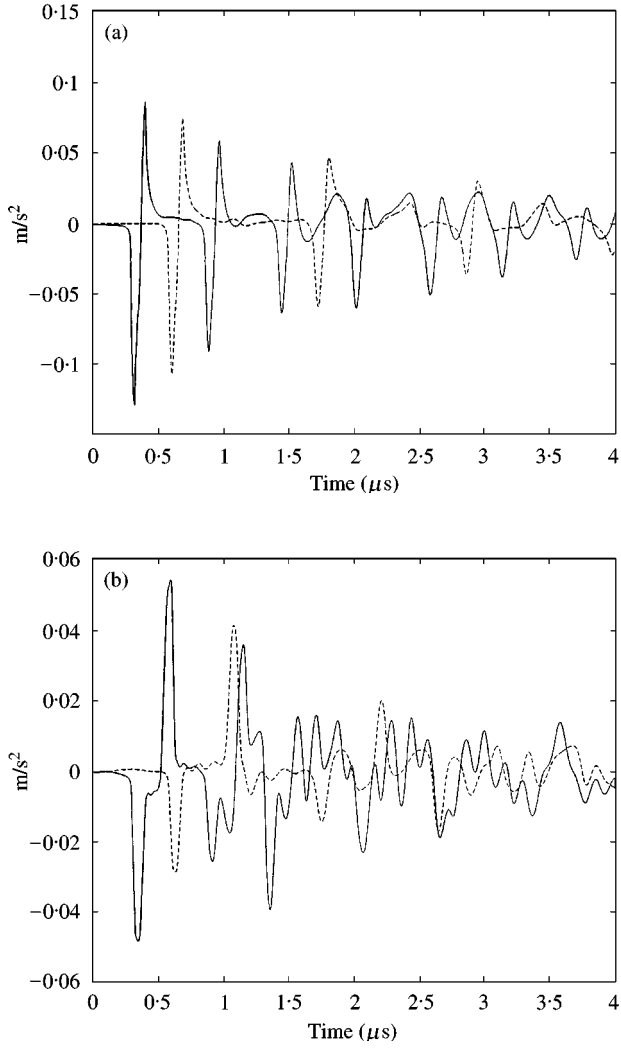

Figure 7. Acceleration versus time (a) in the z direction (b) in the radial direction r for Systems I (—) and II (····) at station 4.

infinite propagation (phase) speed for thermal waves that is predicted by the diffusion heat transfer model. It is found that the inclusion of the interactions between the thermal and mechanical effects results in (1) a new highly attenuated mode, and (2) a very small attenuation in the pressure (P) wave mode; the shear mode is unaffected since, in the model, the thermal-elastic coupling is through volumetric change. In the current work, no transient temperature result is presented; however, preliminary work has indicated that the temperature increase on the surface is low compared to the melting point of the layer material.

The transfer matrix is obtained in closed form and is represented in a similarity transform form. With this representation, the condition number of the transfer

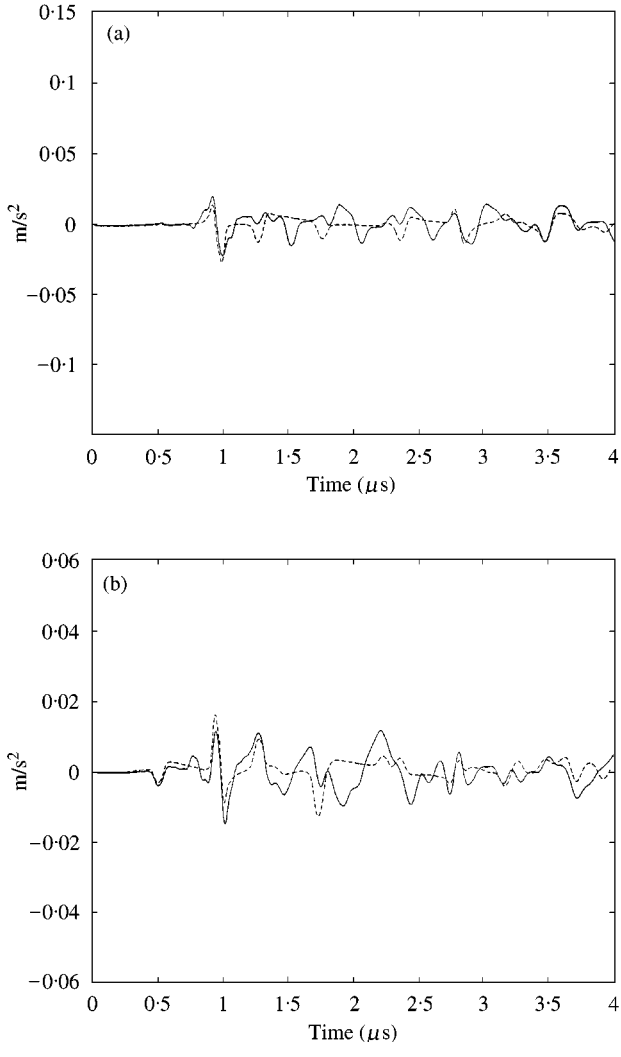

Figure 8. Acceleration versus time (a) in the z direction (b) in the radial direction r for Systems I (—) and II (····) at station 5.

matrix can easily be calculated and, consequently, the inherent numerical instability (loss of precision) in hyperbolic wave propagation problems could be monitored and controlled. This regulation will be even more important in the thermoelastic analysis of layered structures.

It is observed that the acceleration level can reach as high as $10^9\,\mathrm{m/s^2}$ and the effect of layer thickness diminish as the distance between the beam location and the station point is increased. This observation suggests that for these particular layers surface waves play an important role in acceleration. However, it is noteworthy that no material damping mechanism is present in the current formulation, and it is known that material damping can significantly reduce the peak acceleration levels (e.g., see reference [22] for its effect on composites).

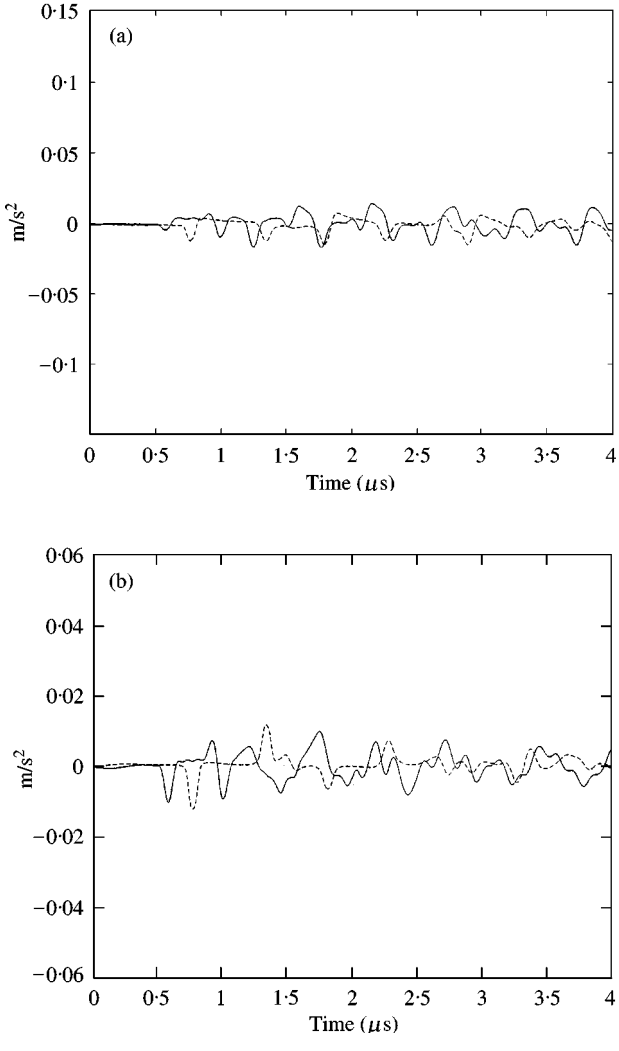

Figure 9. Acceleration versus time (a) in the z direction (b) in the radial direction r for Systems I (—) and II (····) at station 6.

Acceleration levels computed in the current work are high enough to remove particles as small as submicron level with a laser with common pulse energy. It is possible that by utilizing the superposition principle, even a higher level of acceleration can be achieved by multiple heating patterns provided that the surface deformations initiate no surface cracks. No local rotation of the surface is taken into account in the current study. It is possible that rotation could substantially increase the acceleration levels (due to the angular momentum). It is known that the rolling motion due to the angular acceleration of particles increases the cleaning effectiveness (e.g., see references [1, 2]).

The formulation and simulations can be used in relating the acceleration levels to bond (adhesion) forces, and particle radius. The inverse problem, namely, the study

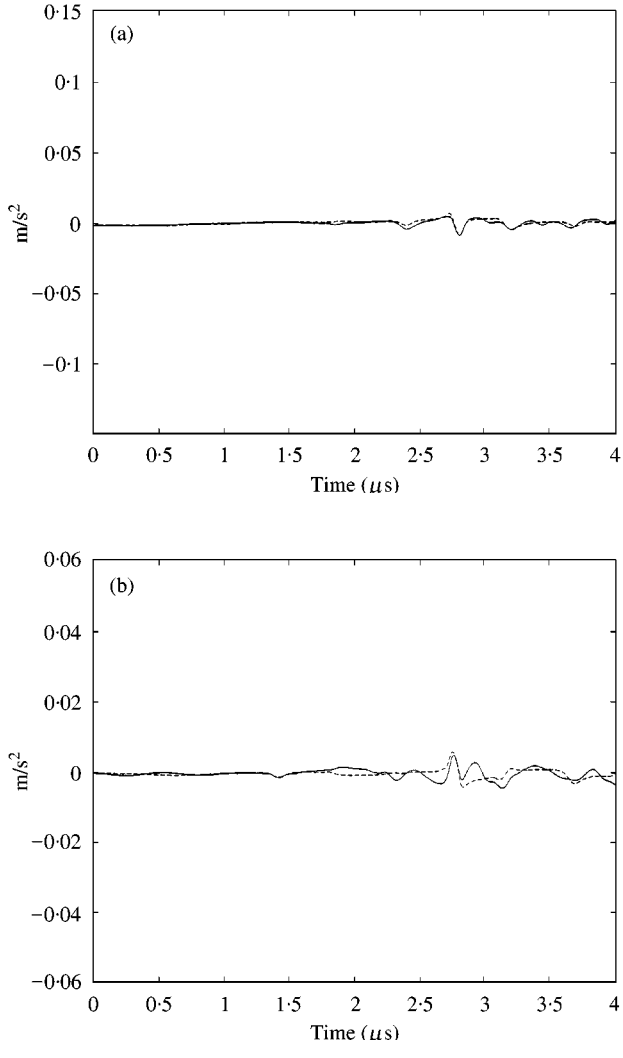

Figure 10. Acceleration versus time (a) in the z direction (b) in the radial direction r for Systems I (—) and II (····) at station 7.

of the characteristics of the adhesion between the surface and particle, can also be of practical interest. The current formulation along with experimental interferometric data can be used in a detailed characterization of bonding for various surface and particle types and materials.

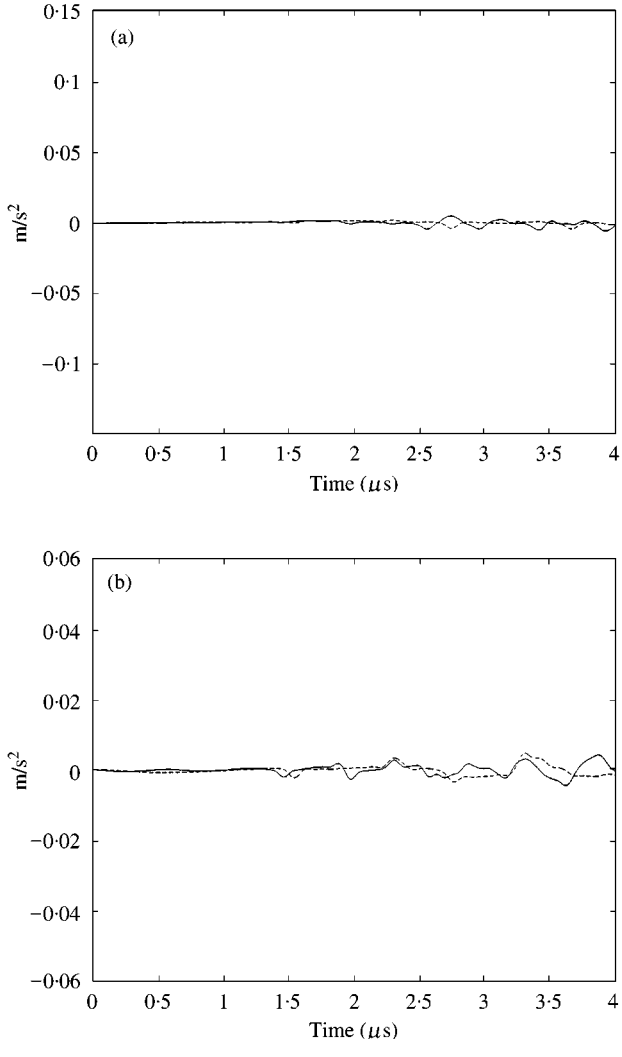

Figure 11. Acceleration versus time (a) in the z direction (b) in the radial direction r for Systems I (—) and II (····) at station 8.

REFERENCES

1. M. Soltani, G. Ahmadi, R. G. Bayer and M. A. Gaynes 1995 *Journal of Adhesion Science and Technology* **9**, 453–473. Particle detachment mechanisms from rough surfaces under substrate acceleration.
2. M. Soltani, and G. Ahmadi, 1995 *Journal of Adhesion Science and Technology* **51**, 105–123. Particle detachment from rough surfaces in turbulent flows.
3. H. W. Lord and Y. Shulman 1967 *Journal of the Mechanics and Physics of Solids* **15**, 299–309. A generalized dynamical theory of thermoelasticity.
4. B. A. Boley 1972 *Nuclear Engineering and Design* **18**, 377–399. Survey of recent developments in the fields of heat conduction in solids and thermoelasticity.

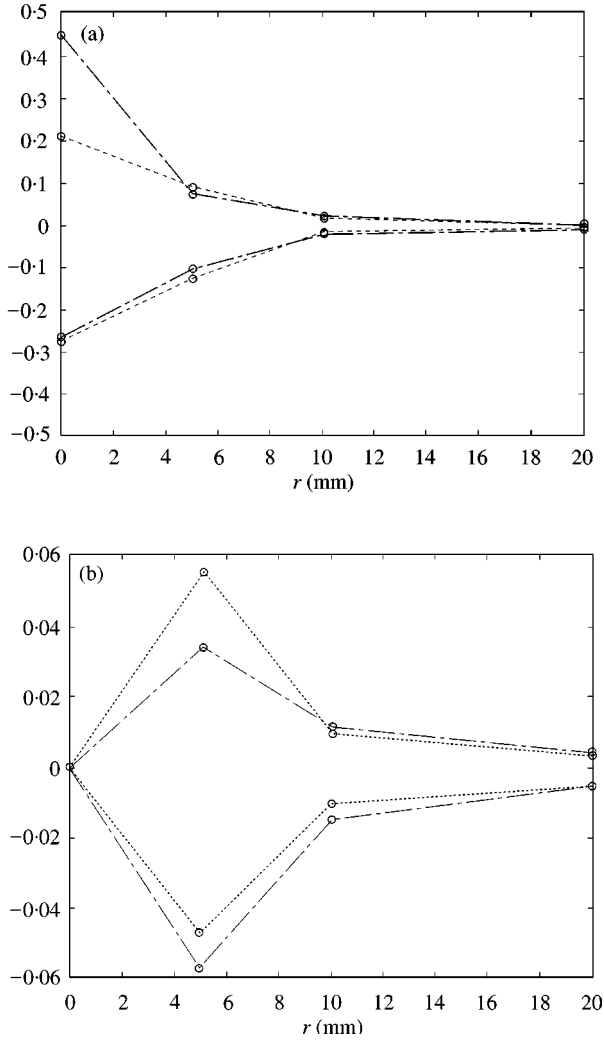

Figure 12. Local maximum and minimum acceleration levels (a) in the z direction (b) in the radial direction r at points 1–8 for System I: –·–, top surface; – – –, bottom surface.

5. D. S. Chandrasekharaiah 1986 *Applied Mechanics Reviews* **39**, 355–376. Thermoelasticity with second sound: a review.
6. D. D. Joseph and L. Preziosi 1989 *Reviews of Modern Physics* **61**, 41–73. Heat waves.
7. D. D. Joseph and L. Preziosi 1990 *Reviews of Modern Physics* **62**, 375–391. Addendum to the paper heat waves.
8. D. S. Chandrasekharaiah 1998 *Applied Mechanical Reviews* Part 1 **51**, 705–729. Hyperbolic thermoelasticity: a review of recent literature.
9. C. Sve and J. Miklowitz 1973 *Journal of Applied Mechanics* March, 161–167. Thermally induced stress waves in an elastic layer.
10. J. B. Spicer 1991 *Ph.D. Dissertation*, Johns Hopkins University. Laser ultrasonics in finite structures: comprehensive modelling with supporting experiment.

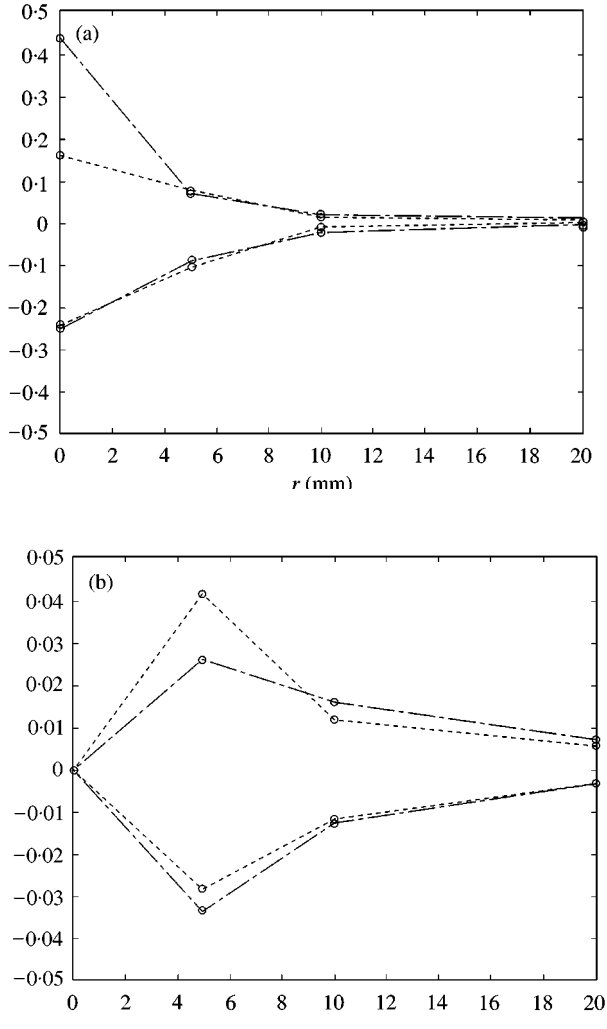

Figure 13. Local maximum and minimum acceleration levels (a) in the z direction (b) in the radial direction r at points 1–8 for System II: $-\cdot-$, top surface; $---$, bottom surface.

11. C. CETINKAYA and A. F. VAKAKIS 1996 *Journal of Sound and Vibration* **194**, 389–416. Transient axisymmetric stress wave propagation in weakly coupled layered structures.
12. T. KUNDU and A. K. MAL 1985 *Wave Motion* **7**, 459–471. Elastic waves in a multilayered solid due to a dislocation source.
13. A. K. MAL 1988 *Wave Motion* **10**, 257–266. Wave propagation in layered composite laminates under periodic surface loads.
14. W. T. THOMSON 1950 *Journal of Applied Physics* **21**, 89–93. Transmission of elastic waves through a stratified solid medium.
15. N. A. HASKELL 1953 *Bulletin of the Seismological Society of America* **54**, 17–34. The dispersion of surface waves on multilayered media.
16. D. J. MEAD 1996 *Journal of Sound and Vibration* **190**, 495–524. Wave propagation in continuous periodic structures: research contributions from Southampton, 1964–1995.

17. Al. A. Kolomenskii and H. A. Schuessler 1998 *Journal of Applied Physics* **84**, 2404–2410. Interaction of laser-generated surface acoustic pulses with fine particles: surface cleaning and adhesion studies.
18. J. H. Lee and C. P. Burger 1995 *Computers and Structures* **54**, 499–514. Finite element modeling of laser-generated lamb waves.
19. J. C. Maxwell 1867 *Philosophical Transactions of the Royal Society* **157**, 49–88. On the dynamical theory of gases.
20. V. Peshkov 1944 *Journal of Physics*, U.S.S.R. **8**, 131. Second sound in He II (in Russian).
21. M. Chester 1963 *Physical Review* **131**, 2013–2015. Second sound in solids.
22. A. K. Mal, Y. Bar-Cohen and S.-S. Lih 1992 *Wave Attenuation in Fiber-Reinforced Composites*, (V. K. Kinra and A. Wolfenden, editors), 245–261. ASTM STP 1169. American Society for Testing Materials.